Wave propagation in 3-D spherical sections: effects of subduction zones

Heiner Igel, Tarje Nissen-Meyer, Gunnar Jahnke
Institut für Geophysik, Ludwig-Maximilians-Universität München, Germany

Submitted to ***Physics of the Earth and Planetary Interiors***
This version printed 2.8.2001.

Abstract

In order do understand details in the seismic wave field observed on regional and global scales on the Earth's surface accurate modeling of 3-D wave propagation is necessary. While numerical techniques are now routinely applied to local seismic wave propagation, only recently the possibility of simulating wave propagation on larger scales in spherical geometry has been investigated. We apply a high-order staggered-grid finite-difference scheme to the elastic wave equations in spherical coordinates [φ,θ,r]. Using regular grid spacing in a single domain the physical space is limited to spherical sections which do not include the axis θ=0. While the staggering of the space-dependent fields improves the overall accuracy of the scheme, some of the tensor elements have to be interpolated to the required grid locations. By comparing with quasi-analytical solutions for layered Earth models we demonstrate the accuracy of the algorithm. Finally, the technique is used to study the effects of a source located in a simplified slab structure. The 3-D technique will allow us to study the wave field due to laterally heterogeneous structures such as subduction zones, plumes or oceanic ridges.

Keywords: wave propagation, subduction zones, finite differences, spherical coordinates, parallel algorithms

Introduction

Many questions on the dynamics of the Earth's interior depend on structural imaging using seismic tomography. While ray-theory based techniques offer the

reconstruction of the long-wavelength structures explaining predominantly phase effects, it is desirable to be able to investigate frequency-dependent wave form effects of 3D structures due to scattering. This applies particularly to the most laterally heterogeneous areas of the mantle, the upper part with subduction zones, ridge structures and plumes and the lower part with the strongly heterogeneous lowermost mantle structure (D") the origin of which is still not well understood. With 3-D reference Earth models in sight, the development of methods which allow the accurate simulation of the complete wave field on regional and global scales is an important step towards understanding the complexity of the observed seismic motion.

Numerical methods have been applied successfully to wave propagation problems on local scales (e.g. Graves, 1993, 1998; Olsen and Archuleta, 1996) using discretizations of the equations of motion in cartesian coordinates. Particularly the finite-difference method played an important role due to its simplicity and the ease with which it is implemented on parallel hardware. The early work of Virieux (1986) in two dimensions was soon extended to 3-D (Witte and Richards, 1987; Mora, 1989), and anisotropic media (Igel et al., 1995). Other approaches include the pseudo-spectral method (e.g. Kosloff et al., 1984; Reshef et al., 1988; Tessmer and Kosloff, 1994; Tessmer, 1995, Furumura et al., 1998), the finite-element method (e.g. Padovani et al., 1994) and a combination of pseudo-spectral and finite-element methods, the spectral element method (e.g. Priolo and Seriani, 1991; Komatitsch, et al., 2000).

A pioneering application of numerical techniques to wave propagation in spherical geometry was carried out by Alterman et al. (1970) using a centered finite-difference technique to solve the problem of P-SV wave propagation in spherical coordinates in the axi-symmetric approximation. Along similar lines - but using high-order approaches and staggered-grid techniques - Igel and Weber (1995, 1996) studied global wave propagation (SH, and P-SV waves, respectively) and investigated the effects of heterogeneous mantle structures. Chaljub and Tarantola (1997) studied topographic effects of the upper mantle discontinuities using a finite-difference algorithm for SH waves (axi-symmetric approach). These discrete grid models allowed the investigation of waveform effects of slab structures (Igel and Ita, 1997), and finite-frequency effects of statistical upper mantle models (Igel and Gudmundsson, 1997). A multi-domain technique allowing waves to be simulated in a complete sphere (axi-symmetric approach) was presented by Thomas et al. (2000)

with applications to scatterers in the lower mantle and their effects on the PKP phase.

Standard regular grid methods like the finite-difference method can not directly be applied to model wave propagation in a complete sphere due to the singularities present in the equations of motion in spherical coordinates. However, when the physical domain is restricted to a spherical section away from the poles, then standard techniques can be used. Igel (1999) presented a pseudo-spectral solution to this problem on a centered grid using the Chebyshev technique previously applied to cartesian systems (e.g. Tessmer and Kosloff, 1994). While the pseudo-spectral method has advantages concerning the accuracy of the spatial differential operators, the method is more difficult to implement on parallel hardware due to the global communication schemes required to perform Fourier transforms (or matrix-matrix multiplies). Therefore, we investigate the possibility of using a high-order staggered-grid method to numerically solve wave propagation in a spherical section.

In the following we first present the governing equations and their numerical solution algorithm. We then discuss the accuracy of the algorithm and show examples of 3-D wave propagation through models with a simple subduction zone structure in the upper mantle.

Governing equations

As we intend to solve the governing time-dependent partial differential equations with a staggered-grid finite-difference method a first-order description of the equations as previously used in cartesian coordinates (e.g. Virieux, 1986, Tessmer and Kosloff, 1994, Tessmer, 1995) seems appropriate. In spherical coordinates [θ,φ,r] the equations of motion for elastic anisotropic wave propagation read

$$
\begin{aligned}
\rho\partial_t v_\theta &= \partial_r\sigma_{r\theta} + \frac{1}{r}\partial_\theta\sigma_{\theta\theta} + \frac{1}{r\sin\theta}\partial_\varphi\sigma_{\varphi\theta} + \frac{1}{r}\left(\left[\sigma_{\theta\theta} - \sigma_{\varphi\varphi}\right]\cot\theta + 3\sigma_{r\theta}\right) + f_\theta \\
\rho\partial_t v_\varphi &= \partial_r\sigma_{r\varphi} + \frac{1}{r}\partial_\theta\sigma_{\theta\varphi} + \frac{1}{r\sin\theta}\partial_\varphi\sigma_{\varphi\varphi} + \frac{1}{r}\left(3\sigma_{r\varphi} + 2\sigma_{\varphi\theta}\cot\theta\right) + f_\varphi \\
\rho\partial_t v_r &= \partial_r\sigma_{rr} + \frac{1}{r}\partial_\theta\sigma_{r\theta} + \frac{1}{r\sin\theta}\partial_\varphi\sigma_{r\varphi} + \frac{1}{r}\left(2\sigma_{rr} - \sigma_{\theta\theta} - \sigma_{\varphi\varphi} + \sigma_{r\theta}\cot\theta\right) + f_r
\end{aligned}
\qquad (1)
$$

where v_i are the components of velocity, ρ is the mass density, σ_{ij} are the components of the stress tensor, and f_i are the force components. In general anisotropic media the stress-strain relation is given as

$$\sigma_{ij} = c_{ijkl}\varepsilon_{kl} + M_{ij} \qquad (2)$$

where c_{ijkl} are the components of the fourth-order elasticity tensor, ε_{kl} are the components of the deformation tensor, and M_{ij} are the components of the source moment tensor. The deformation rate is related to the velocities by

$$\begin{aligned}
\partial_t \varepsilon_{\theta\theta} &= \frac{1}{r}\left(\partial_\theta v_\theta + v_r\right) \\
\partial_t \varepsilon_{\varphi\varphi} &= \frac{1}{r\sin\theta}\partial_\varphi v_\varphi + \frac{1}{r}v_r + \frac{\cot\theta}{r}v_\theta \\
\partial_t \varepsilon_{rr} &= \partial_r v_r \\
\partial_t \varepsilon_{\varphi r} &= \frac{1}{2}\left(\frac{1}{r\sin\theta}\partial_\varphi v_r + \partial_r v_\varphi - \frac{1}{r}v_\varphi\right) \\
\partial_t \varepsilon_{\theta r} &= \frac{1}{2}\left(\frac{1}{r}\partial_\theta v_r + \partial_r v_\theta - \frac{1}{r}v_\theta\right) \\
\partial_t \varepsilon_{\theta\varphi} &= \frac{1}{2}\left(\frac{1}{r\sin\theta}\partial_\varphi v_\theta + \frac{1}{r}\partial_\theta v_\varphi - \frac{\cot\theta}{r}v_\varphi\right) \quad . \qquad (3)
\end{aligned}$$

The elasticity parameters are conveniently described in the condensed notation

$$\sigma_p = c_{pq}\varepsilon_q \qquad p,q = 1,...,6 \quad (4)$$

where - in spherical coordinates - the mapping: $1\rightarrow\theta\theta$, $2\rightarrow\varphi\varphi$, $3\rightarrow rr$, $4\rightarrow\varphi r$, $5\rightarrow\theta r$, $6\rightarrow\theta\varphi$ applies. The corresponding elements of the elasticity tensor are then given by

$$\begin{pmatrix} \sigma_{\theta\theta} \\ \sigma_{\varphi\varphi} \\ \sigma_{rr} \\ \sigma_{\varphi r} \\ \sigma_{\theta r} \\ \sigma_{\theta\varphi} \end{pmatrix} = \begin{pmatrix} \mathbf{c_{\theta\theta\theta\theta}} & \mathbf{c_{\theta\theta\varphi\varphi}} & \mathbf{c_{\theta\theta rr}} & c_{\theta\theta\varphi r} & c_{\theta\theta\theta r} & c_{\theta\theta\theta\varphi} \\ \mathbf{c_{\theta\theta\varphi\varphi}} & \mathbf{c_{\varphi\varphi\varphi\varphi}} & \mathbf{c_{\varphi\varphi rr}} & c_{\varphi\varphi\varphi r} & c_{\varphi\varphi\theta r} & c_{\varphi\varphi\theta\varphi} \\ \mathbf{c_{\theta\theta rr}} & \mathbf{c_{\varphi\varphi rr}} & \mathbf{c_{rrrr}} & c_{rr\varphi r} & c_{rr\theta r} & c_{rr\theta\varphi} \\ c_{\theta\theta\varphi r} & c_{\varphi\varphi\varphi r} & c_{rr\varphi r} & \mathbf{c_{\varphi r\varphi r}} & c_{\varphi r\theta r} & c_{\varphi r\theta\varphi} \\ c_{\theta\theta\theta r} & c_{\varphi\varphi\theta r} & c_{rr\theta r} & c_{\varphi r\theta r} & \mathbf{c_{\theta r\theta r}} & c_{\theta r\theta\varphi} \\ c_{\theta\theta\theta\varphi} & c_{\varphi\varphi\theta\varphi} & c_{rr\theta\varphi} & c_{\varphi r\theta\varphi} & c_{\theta r\theta\varphi} & \mathbf{c_{\theta\varphi\theta\varphi}} \end{pmatrix} \begin{pmatrix} \varepsilon_{\theta\theta} \\ \varepsilon_{\varphi\varphi} \\ \varepsilon_{rr} \\ \varepsilon_{\varphi r} \\ \varepsilon_{\theta r} \\ \varepsilon_{\theta\varphi} \end{pmatrix} \qquad (5)$$

and they reduce to

$$\begin{aligned}
\boldsymbol{c_{\theta\theta\theta\theta}} &= \boldsymbol{c_{\varphi\varphi\varphi\varphi}} = \boldsymbol{c_{rrrr}} = \lambda + 2\mu \\
\boldsymbol{c_{\theta\theta\varphi\varphi}} &= \boldsymbol{c_{\theta\theta rr}} = \boldsymbol{c_{\varphi\varphi rr}} = \lambda \\
\boldsymbol{c_{\varphi r\varphi r}} &= \boldsymbol{c_{\theta r\theta r}} = \boldsymbol{c_{\theta\varphi\theta\varphi}} = \mu \qquad (6)
\end{aligned}$$

in the isotropic elastic case, where λ and μ are the Lamé constants and all other elements are zero.

In the following we will present a numerical solution to these equations for the isotropic case based on a staggered-grid finite-difference method.

Numerical solution

All space-dependant fields (velocities, stresses, material parameters) are defined on an equidistant grid in spherical coordinates [θ,φ,r]. As mentioned above, due to the singularities present in the equations of motion, the physical domain is limited to regions away from the axis θ=0, where motion is not defined. A convenient choice is to center the spherical section around the equator. In Figure 1 a spherical section with angular ranges 80^o (for both φ and θ) is shown with a depth extent of 5000km. Centering the domain around the equator minimizes the range of grid increments on the spherical shell thus optimizing the stability for a particular model range.

The first-order formulation of the equations of motion suggests the use of a staggered-grid scheme as applied in several cartesian algorithms (e.g. Virieux, 1986; Graves, 1993; Frankel, 1993; Igel et al., 1995; Olsen et al., 1995). The staggering of the vector and tensor elements as well as the material parameters is shown in Figure 2. Note that due to the spherical coordinate system geometrical terms appear in the equations and r and θ need to defined at all the staggered locations. The finite-difference operators are convolutional operators as used by Igel et al. (1995). In the numerical tests carried out below a 4-point operator is being applied. The time extrapolation is carried out by a first-order Taylor expansion.

We define the material parameters (ρ and tensor of elastic constants c_{pq}) at the grid locations where the diagonal elements of the stress tensor are defined. This implies that those parameters which are needed elsewhere in the grid cell have to be interpolated to these locations. This interpolation is carried out using a second order scheme. To accurately model the location of interfaces or sources at material discontinuities such interpolations are necessary (e.g. Igel et al., 2001). In comparison with cartesian schemes a further complication occurs: as can be seen from equations (1) and (3) the staggering does not lead to a completely decoupled scheme as the calculation of velocity or stress components requires terms which are not defined or centered at the corresponding grid locations. For example, to calculate the acceleration v_θ (left-hand side of the top equation (1)) the stress components

$\sigma_{\theta\theta}$, $\sigma_{\varphi\varphi}$, $\sigma_{\rho\theta}$ need to be interpolated to the location of v_θ. These interpolations are carried out using a second-order scheme.

The free surface boundary condition

$$\sigma_{rr} = \sigma_{r\varphi} = \sigma_{r\theta} = 0 \qquad (7)$$

is implemented in the same way as in the case of a cartesian system by using an explicit method based on (anti-)symmetry conditions as suggested by Graves (1996). Simple absorbing boundary conditions are implemented by tapering the fields as well as seismic velocities with decreasing values using Gaussian functions. There are two grid levels at which the free surface can be defined (at the level of the diagonal stress elements or the level of the radial velocity component). Note that Gottschämmer and Olsen (2001) investigated these two options and concluded that the overall errors are smaller when the free surface is defined at the latter location, which is the approach we adopted. The computationally demanding algorithm is implemented using domain decomposition in the vertical direction and the message passing interface (MPI). Hereby, the 3D grid is divided into *n* depth sections, where n is the number of computational nodes. To be able to calculate the space derivatives with respect to the vertical direction across the domain boundaries *nop*/2 grid slices have to be communicated to the neighboring processor, where *nop* is the length of the differential operator (in our case *nop*=4). Typical performance data for a model of size 720x1220x406 and a simulation run for 4200 time steps are a memory requirement of ca. 60GBytes and a runtime of 10.5 hours on 13 nodes of a Hitachi Sr8000-F1.

Verification, Accuracy, Snapshots

To assess the accuracy of the proposed algorithm we compare the numerical solutions with synthetic seismograms calculated with the reflectivity method (Fuchs and Müller, 1971; Wang, 1999) for regional wave propagation. The model parameters are v_P=8.08km/s, v_S=4.47km/s, and ρ=3.37g/cm^3. The grid size is 200^3 (θ,φ,r) and the grid distance at the Earth's surface is approximately 4km, leading to a cube of 800km side length. The source is a vertical point force f_r acting at a depth of 100km. 600 time steps were evaluated with a time increment of 0.2 seconds. We simulate a delta-like point source in space and time at the corresponding grid location. This leads to synthetic seismograms containing numerical artifacts which

are reduced through convolution with a source time function of appropriate dominant frequency. The source-time function is the first derivative of a Gaussian.

In Figure 3 synthetic seismograms (vertical velocity component) are shown for epicentral distances up to 400km using both the reflectivity method and the finite-difference algorithm. The reflectivity seismograms have been calculated with the Earth-flattening transformation. We calculate the energy misfit ε of the waveforms for a particular velocity component *v* summing over samples *i*

$$\varepsilon = \frac{\sum_i (v_i^{FD} - v_i^{REF})^2}{\sum_i v_i^{REF\,2}} \quad . \quad (8)$$

The misfit is shown in Figure 4 as a function of dominant period and distance. As expected the error generally decreases with increasing dominant period as the wave field is sampled with a larger number of grid points per wavelength. The error also increases with propagation distance. For a dominant period of 20 seconds (this corresponds to approx. 22 points per dominant wavelength) the error is below 1% for distances smaller than 350km.

Seismograms are compared for a two-layer model in Figure 5 (vertical velocity component). The grid size is the same as for the homogeneous model. The top layer has the same properties as mentioned above. Below 240km depth the material parameters are v_p=8.89km/s, v_S=4.92km/s, and ρ=3.7g/cm^3. The source is an explosion at 100km depth. 900 time steps were evaluated with a time increment of 0.2 seconds. The comparison with the reflectivity seismograms shows that all signals are present in the numerical solution. The reflections and conversions from the discontinuity are labeled with letter *g*. Ray-theoretical arrival times were calculated using a Gaussian beam method and superimposed on the seismograms. The misfit energy as functions of distance and frequency (Figure 6) shows that for this setup at a dominant period of 20 seconds the misfit is approximately 1% for all epicentral distances.

Snapshots for wave propagation simulation on a 200^3 grid are shown in Figure 7 at four different times. The physical domain is 90^ox90^ox5000km. The source is an explosion at 600km depth and the dominant period of the wave field is approximately 40 seconds. The simulation was carried out for the spherically symmetric PREM model (isotropic part, no crust). The snapshots show predominantly the direct P

waves and the surface reflections and conversions (pP, pS) as well as the core-mantle boundary reflections (PcP, PcS).

Numerical Example: slab effects

Subducted lithosphere constitutes the strongest laterally heterogeneous structures in the Earth's upper mantle and it hosts the largest earthquakes on this planet. The wave field radiated by seismic sources inside subduction zones may be severely affected by their heterogeneous structure. In addition to the high-velocity anomaly associated with a cool slab, low-velocity layers due to untransformed oceanic crust at the top of the slab may exist (e.g. Hori et al., 1985), possibly containing water (Ihmlé and Madariaga, 1996). The effects of subduction zones on seismic waveforms and arrival times were previously investigated by Vidale (1987), Cormier (1989), Weber, (1990), Vidale et al. (1991), Bostock et al. (1993), and Sekiguchi (1992). Shapiro et al. (2000) studied wave effects of accretionary prisms with evidence from long-period surface waves propagating along the trench. As an application of our algorithm we investigate the effects of a subduction zone structure for an earthquake source inside a low-velocity layer at the top of the slab.

The background model is the isotropic part of PREM (Dziewonski and Anderson, 1981) without the crustal layers. The model with grid size 720x1200x406 has a lateral extent of 22^0 and 13^0 in $\varphi-$ and θ-directions, respectively. The maximum depth is 808km. The S-velocity model is shown in Figure 8. The slab has a maximum positive velocity perturbation of 8% and horizontal width of approx. 100km. A low-velocity layer is located on top of the slab with a maximum negative perturbation of 4% and a width of 20km. Please note that the thickness of this layer has been imposed through the still relatively coarse grid spacing. The source (black star) is located at 260km depth and is a dip slip source with strike $\Phi_s=0^o$, rake $\lambda=90^o$, and the fault plane (and the slab) dips at $\delta=52^o$ at the source location. The slab is invariant in θ-direction. We situate a receiver profile across the slab (in φ-direction) directly above the source and a receiver semi-ring around the epicenter at a distance of 5^o. The receiver strings are schematically shown in Figure 9. In all subsequent seismogram plots the moment rate function is a Gauss function with dominant period of 6 seconds.

Snapshots of the simulation of wave propagation through the slab structure are shown in Figure 10. We focus on shear wave propagation and show the curl

component perpendicular to the particular model faces. The shear energy propagating in the slab direction (upwards and downwards) is characterized by an additional phase developing due to the low-velocity structure. In addition, at the top of the slab both these shear waves are reflected in eastern direction. The vertical component of velocity along a profile across the subduction zone is shown in Figure 11. The time window displayed contains predominantly the direct S-wave arrival. The waves traveling upwards through the slab are advanced several seconds (negative distances) while the waves propagating away from the slab are unaffected (positive distances). Most noticeable are additional phases recorded at distances around -2^o in the wake of the direct arrival. Due to the slab there is a sudden decrease in amplitude at around -3^o indicating the edge of the high-velocity structure at the surface.

The vertical component of motion recorded on a semi-ring at 5^o distance from the epicenter is shown in Figure 12. The P-wave arrives at approx. 75 seconds and the S-wave at 140 seconds. The slab has strong effects on relative amplitudes and wave forms of both these arrivals: (1) The amplitudes of the P-wave for azimuths greater 100^o (away from the slab) are not affected. However, for propagation in the direction of the slab the amplitudes are reduced by up to 50%. In case these signals are used to determine the source mechanism errors may occur. (2) The S-waves are severely affected in the azimuthal range 0^o-80^o. This corresponds to waves propagating inside the slab. The S-pulse is advanced, broadened (i.e. two distinct phases) and the amplitude reduced. (3) In addition, a diffracted S-wave is propagating in easterly direction away from the slab. The transverse component of motion recorded on the semi-ring of receivers further highlights the effects of the slab (Figure 13). Within a very small azimuthal range (at azimuths 60^o and 80^o) the wave form of the S-arrival splits up into two distinct arrivals and a diffracted wave propagates away from the slab. The presence of the slab leads to considerable reduction of the amplitude of the S-wave (azimuths around 20^o).

Discussion

To account for wave field complexities which may occur for waves propagating through strongly heterogeneous regions of the mantle (subduction zones, ridges, lowermost mantle) an accurate modelling of 3-D wave propagation in general heterogeneous structures in spherical geometry is required. In this study we present a staggered-grid finite-difference solution to the isotropic elastic wave equation in

spherical coordinates which is applicable to intermediate epicentral distances (e.g. up to 100^o) as the physical domain is limited to spherical sections excluding the Earth's center and the axis $\theta=0$. The finite-difference approach - in comparison to previous work using pseudo-spectral methods (Igel, 1999) - offers advantages concerning the implementation of the algorithm on parallel hardware. Finite difference schemes rely on local operators, thus considerably reducing the amount of communication necessary to calculate the numerical partial derivatives. Such algorithms will for some time remain computational intensive approaches and to tackle realistic problems parallelization is necessary.

In this study we apply a standard finite-difference method which in the future should be extended to incorporate recent advances in the understanding of finite-difference operator accuracy (e.g. Geller and Takeuchi, 1998; Takeuchi and Geller, 2000). Here, the algorithm was compared with quasi-analytical solutions using the reflectivity method. The comparison shows that the body waves are well modeled as long as a sufficiently large number of grid points per wavelength is employed. Further research is needed to carefully investigate the accuracy for surface wave propagation as strong effects for surface wave propagating through subduction zones, plume heads, or along or across ridge axes are to be expected.

We applied this algorithm to simulate waves radiated by a source inside a subducting slab. The slab consists of a maximally 8% positive velocity perturbation and a maximally 4% negative velocity perturbation at the top of the slab. The source is located inside this low-velocity layer. The synthetic seismograms show pronounced effects on the direct P- and S-waves propagating upwards along the slab. With small changes of propagation direction the wave forms and their spectral content changes. The slab also affects the polarities of the first motion. This implies that errors may occur when the source mechanism is estimated using laterally homogeneous models. While the magnitude of these effects may be exaggerated through the thickness of the low-velocity zone, the simulated effects may indicate at least qualitatively what effects are to be expected. Further complications may arise through strongly heterogeneous Q-structure inside the slab. The inclusion of viscoelasticity and anisotropy into the algorithm presented here is work in progress.

These results as well as previous studies show that a systematic investigation of such effects for likely subduction zone structures is necessary. Some of the wave

form effects reported could be used to further constrain the structural details in the upper mantle.

Acknowledgments

We thank the Leibniz Rechenzentrum in Munich for access to their supercomputers. This work is funded by the Deutsche Forschungsgemeinschaft (Ig16/2). We thank Phil Cummins and two anonymous reviewers for constructive comments.

References

Alterman, Z., Aboudi, J., Karal, F.C., 1970. Pulse propagation in a laterally heterogeneous solid elastic sphere. Geophys. J. Roy. Astr. Soc., 21, 243-260.

Anderson, D.L., 1989. Theory of the Earth. Blackwell Scientific Publications.

Bostock, M.G., VanDecar, J.C:, Snieder, R.K., 1993. Modeling teleseismic P-wave propagation in the upper mantle using a parabolic approximation, Bull. Seis. Soc. Amer., 83, 756-779.

Chaljub, E., Tarantola, A., 1997. Sensitivity of SS precursors to topography on the upper-mantle 660-km discontinuity. Geophys. Res. Lett., 24, 2613-2616.

Cormier, V., 1989. Slab diffraction of S-waves, J. Geophys. Res., 94, 3006-3024.

Dziewonski, A.M., Anderson, D.L., 1981. Preliminary Reference Earth Model, Phys. Earth Planet. Int., 25, 297-356.

Frankel, A., 1993. Three-dimensional simulations of ground motions in the San Bernardino Valley, California, for hypothetical earthquakes on the San Andreas Fault, Bull. Seis. Soc. Amer., 83, 1020-1041.

Fuchs, K., Müller, G., 1971. Computation of synthetic seismograms with the reflectivity method and comparison with observations. Geophys. J. Roy. Astr. Soc., 23, 417-433.

Furumura, T., B. L. N. Kennett, H. Takenaka, 1998. Parallel 3-D pseudo-spectral simulation of seismic wave propagation, Geophysics, 63, No 1, 279-288.

Geller, R.J., Takeuchi, N., 1998. Optimally accurate time domain finite difference scheme for the elastic wave equation: one-dimensional case. Geophys. J. Int., 135, 48-62.

Gottschämmer, E., Olsen, K., 2001. Accuracy of the explicit planar free-surface boundary condition implemented in a fourth-order staggered-grid velocity-stress finite-difference scheme, submitted to Bull. Seis. Soc. Am.

Graves, R.W., 1993. Modelling 3-D site response effects in the Marina district basin, San Francisco, Cal., Bull. Seism. Soc. Am., 83, 1042-1063.

Graves, R.W., 1998. 3-D finite-difference modeling of the San Andreas Fault: source parameterization and ground motion levels, Bull. Seism. Soc. Am., 88, 881-897.

Hori, S., Inoue, Y., Fukao, Y., Ukawa, M., 1985. Seismic detection of the untransformed basaltic oceanic crust subducting into the mantle. Geophys. J. Roy. Astr. Soc., 83, 169-197, 1985.

Igel, H., 1999. Wave propagation in spherical sections using the Chebyshev Method, Geophys. J. Int., 136, 559-567.

Igel, H., Riollet, B., Mora, P., 1995. Anisotropic wave propagation through finite difference grids, Geophysics, 60, 1203-1216.

Igel, H., Weber, M., 1995. SH-wave propagation in the whole mantle using high-order finite differences. Geophys. Res. Lett., 22, 731-734.

Igel, H., Weber, M., 1996. P-SV wave propagation in the Earth's mantle using finite-differences: Application to heterogeneous lowermost mantle structure. Geophys. Res. Lett., 23, 415-418.

Igel, H., Gudmundsson, O., 1997. Frequency-dependent effects on travel times and waveforms of long-period S and SS waves. Phys. Earth Planet. Int., 104, 229-246.

Igel, H., Ita, J., 1997. Teleseismic effects of subducting slabs: a numerical study. K. Fuchs (ed.), Upper Mantle Heterogeneities from Active and Passive Seismology, Kluwer Academic Publishers, 333-341.

Igel, H., Jahnke, G., Ben-Zion, Y., 2001. Numerical simulation of fault zone trapped waves: accuracy and 3-D effects, submitted to Pure and Appl. Geoph.

Ihmlé, P.F., Madariaga, R., 1996. Monochromatic body waves excited by great subduction zone earthquakes. Geophys. Res. Lett., 23, 2999-3002.

Komatitsch, D., Barnes, C., Tromp, J., 2000. Simulation of anisotropic wave propagation based upon a spectral element method, Geophysics, 65, 1251-1260.

Kosloff, D., Reshef, M., Loewenthal, D., 1984. Elastic forward modelling by the Fourier method, Geophysics, 49, 634-639.

Montagner J.P., Griot-Pommera, D.A., Lave, J., 2000. How to relate body wave and surface wave anisotropy? J. Geophys. Res., B, 105; 8, 19,915-19,027.

Mora, P., 1989. Modeling anisotropic seismic waves in 3-D, SEG Abstracts. 59, 1039-1043.

Olsen, K.B., Archuleta, R.J., Matarese, J.R.,1995. Magnitude 7.75 earthquake on the San-Andreas fault: three-dimensional ground motion in Los Angeles. Science, 270, 1628-1632.

Padovani, E., Priolo, E., Seriani, G., 1994. Low- and high-order finite-element method: experience in seismic modelling. J. Comp. Acoust., 2, 371-422.

Priolo, E., Seriani, G., 1991. A numerical investigation of Chebyshev spectral element method for acoustic wave propagation. In: Vichnevetsky, R., Ed., Proc. 13th IMACS Conf. On Comp. Appl. Math., Dublin, 551-556.

Reshef, M., Kosloff, D., Mickey, E., Hsiung, C., 1988. 3-D elastic modeling by the Fourier method. Geophysics, 53, 1184-1193.

Sekiguchi, S., 1992. Amplitude distribution of seismic waves for laterally heterogeneous structures including a subducting slab, Geophys. J. Int., 111, 448-464.

Shapiro, N.M., Olsen, K.B., Singh, S.K., 2000. Wave guide effects in subduction zones; evidence from three-dimensional modeling. Geophys. Res. Lett., 27, 433-436.

Smith G.P., Ekstrom G., 1999. A global study of P (sub n) anisotropy beneath continents. J. Geophys. Res., B, 104, 1, 963-980.

Takeuchi, N., Geller, R.J., 2000. Optimally accurate second order time-domain finite-difference scheme for computing synthetic seismograms in 2-D and 3-D media. Phys. Earth Planet. Int., 119, 99-131.

Tessmer, E., 1995. 3-D seismic modelling of general material anisotropy in the presence of the free surface by a Chebyshev spectral method. Geophys. J. Int., 121; 557-575.

Tessmer, E., Kosloff, D., 1994. 3-D elastic modelling with surface topography by a Chebyshev spectral method. Geophysics, 59, 464-473.

Thomas, C., Igel, H., Weber, M., Scherbaum, F., 2000. Acoustic simulation of P-wave propagation in a heterogeneous spherical Earth: Numerical method and application to precursor energy to PKPdf. Geop. J. Int., 141; 307-320.

Vidale, J.E., 1987. Waveform effects of a high-velocity subducted slab, Geoph. Res. Lett., 14, 542-545.

Vidale, J.E., Williams, Q., Houston, H., 1991. Waveform effects of a metastable olivine tongue in subducting slabs, Geoph. Res. Lett., 18, 2201-2204.

Virieux J., 1986. P-SV wave propagation in heterogeneous media: velocity-stress finite-difference method. Geophysics, 51, 889-901.

Weber, M., 1990. Subduction zones – their influence on traveltimes and amplitudes of P-waves, Geop. J. Int., 101, 529-544.

Witte, D., Richards, P.G., 1987. Modeling seismic waves in 2-D and 3-D structures. Yearbook, Lamont-Doherty Observatory, 64-68.

Wang, R., 1999. A simple orthonormalization method for stable and efficient computation of Green's function. Bull. Seis. Soc. Amer., 89, 733-741.

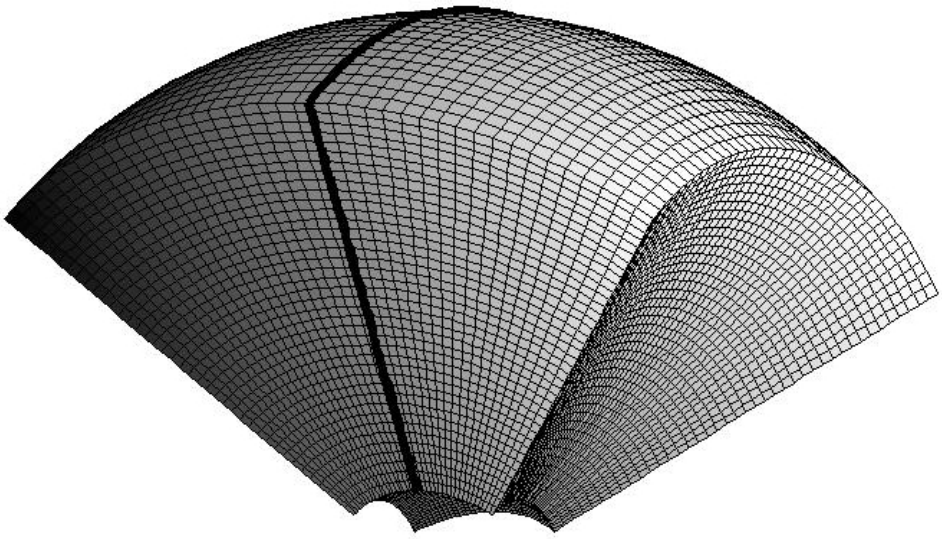

Figure 1: Physical domain for wave field computations. In order to avoid problems with the singularities in the elastic wave equations in spherical coordinates along the axis θ=0 we center the model on the equator (solid lines). Geographical models can be rotated accordingly.

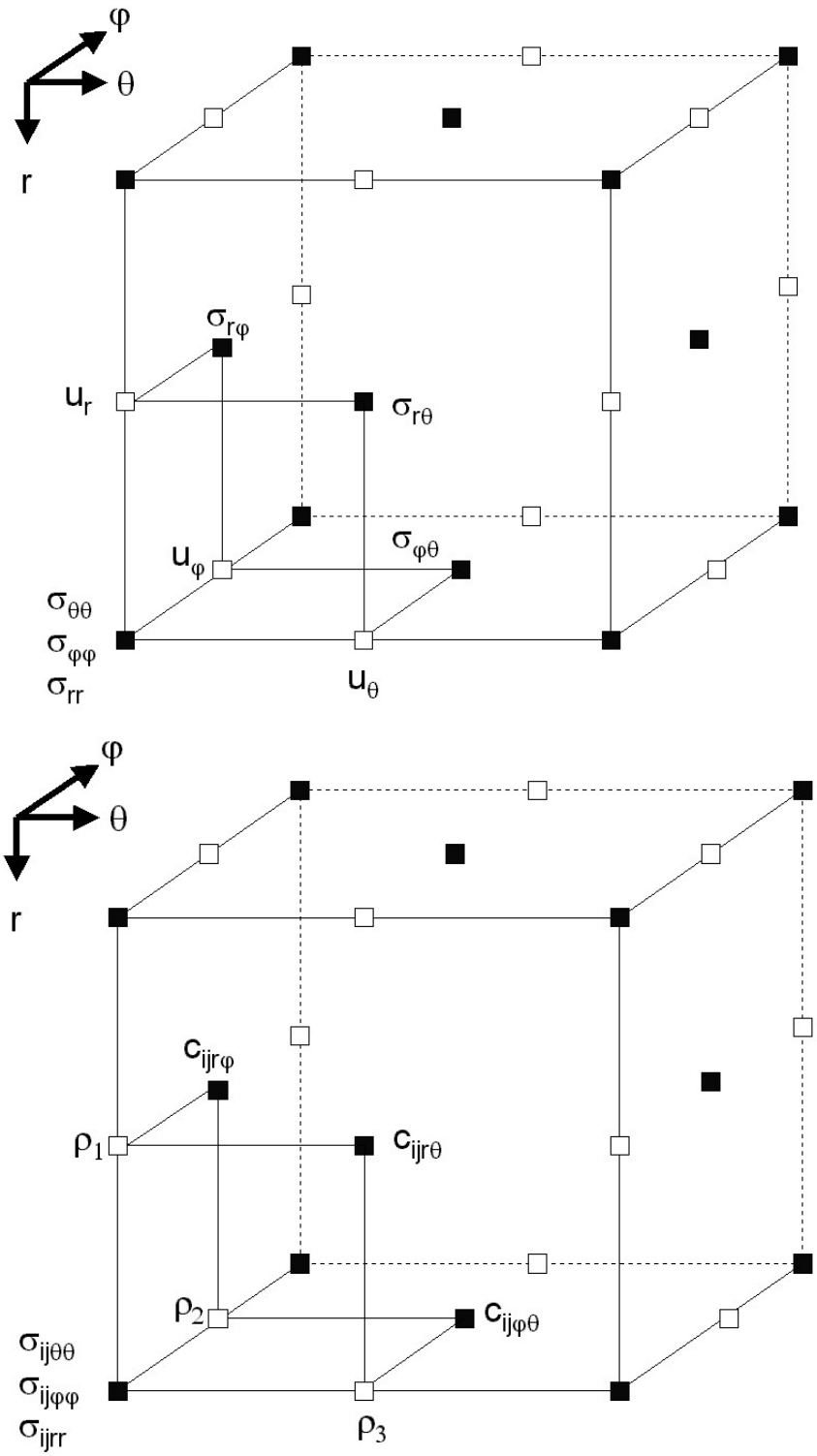

Figure 2: Top: Staggered grid used in the finite-difference calculations. The elements of a cell unit are linked by lines. Note that some of the elements need to be interpolated to calculate the acceleration (see text). **Bottom:** Locations where material parameters are defined. Note that in heterogeneous media the material parameters (e.g. ρ) may vary within a grid cell.

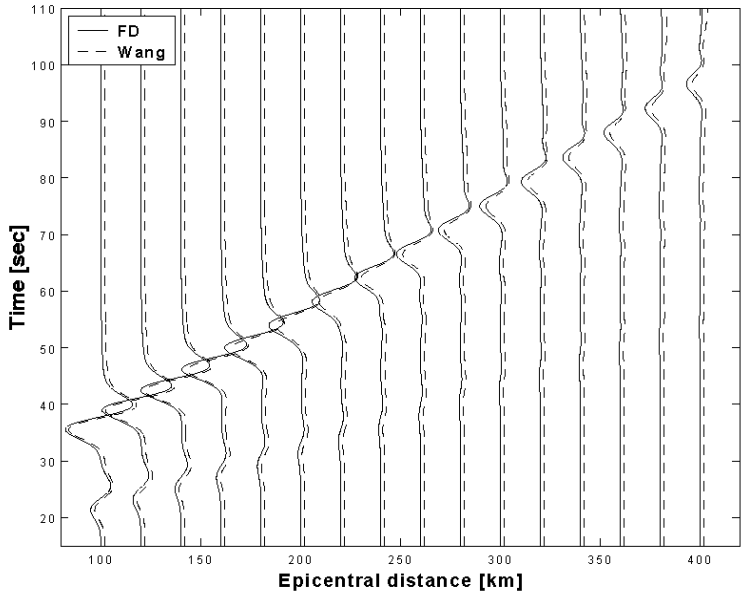

Figure 3: Comparison of synthetic seismograms (vertical velocity component) by the FD method (solid lines) with seismograms calculated using the reflectivity technique (dashed lines, slightly offset) for a homogeneous model (v_p=8.08km/s, v_s=4.47km/s, ρ=3.37g/cm^3). The source is a vertical force at 100km depth. The dominant period is 12 seconds.

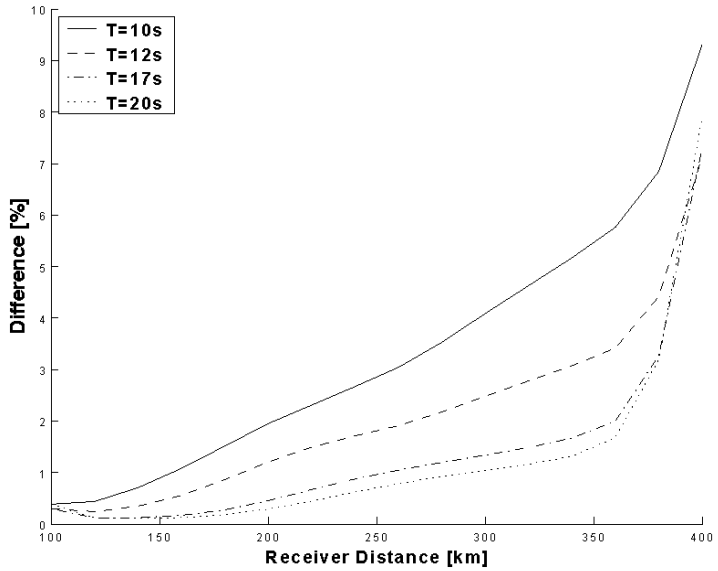

Figure 4: The energy misfit of the traces shown in the previous Figure as a function of receiver distance and dominant period.

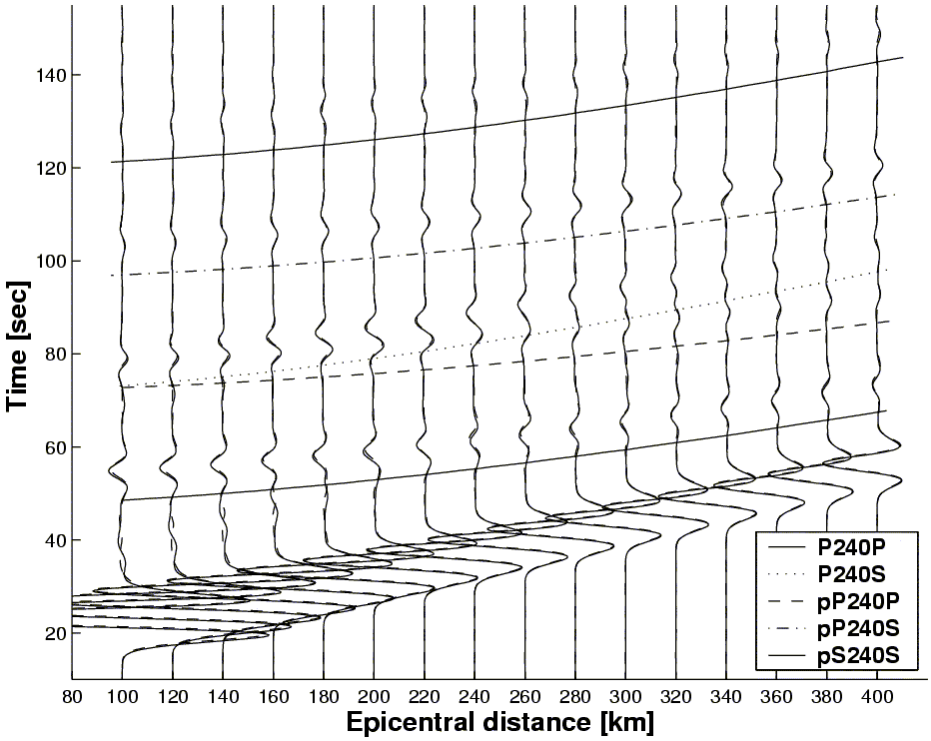

Figure 5: Comparison of synthetic seismograms (vertical velocity component) by the FD method (solid lines) with seismograms calculated using the reflectivity technique (dashed lines on top of solid lines) for a two-layer model (see text) with an interface at 240km depth. The source is an explosion at 100km depth. The dominant period is 12 seconds.

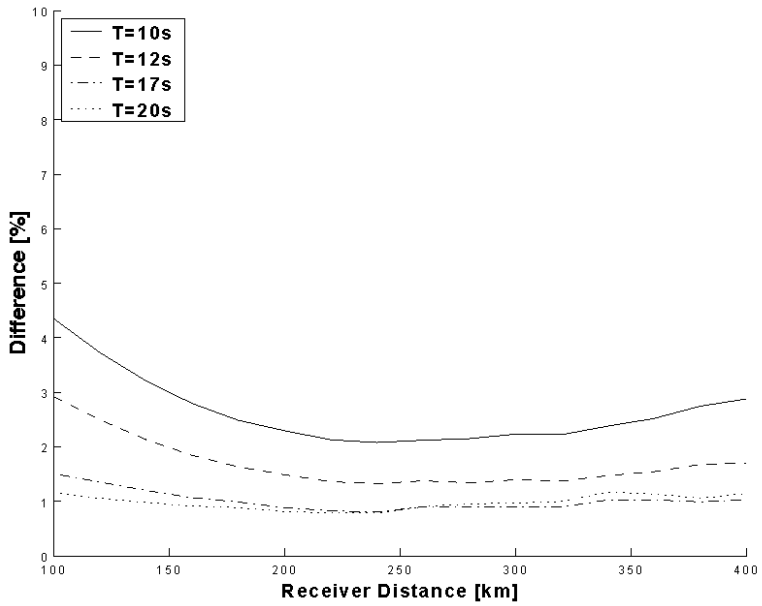

Figure 6: The energy misfit of the traces shown in the previous figure as a function of receiver distance for seismograms with varying dominant frequency.

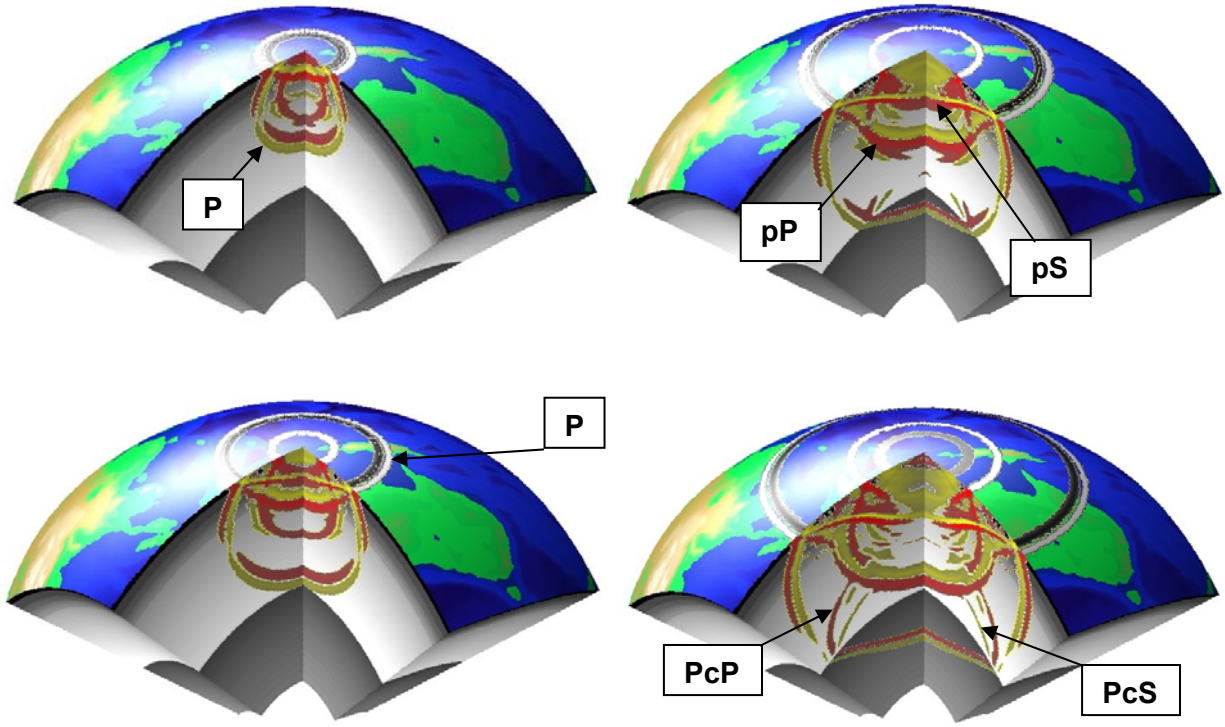

Figure 7: Snapshots of elastic wave propagation for an explosive source at 600km depth. The model is the isotropic part of PREM (no crust). The vertical displacement is shown at four different times: Top left: t=125s. Bottom left: t=200s. Top right: t=260s. Bottom right: t=320s. Red and yellow colors denote positive and negative vertical velocity, respectively. At the surface a gray scale is employed. Only amplitudes larger than 1% of the total wavefield are displayed. The major phases are the direct P wave, pP, pS, PcP, PcS and a P wave entering the outer core.

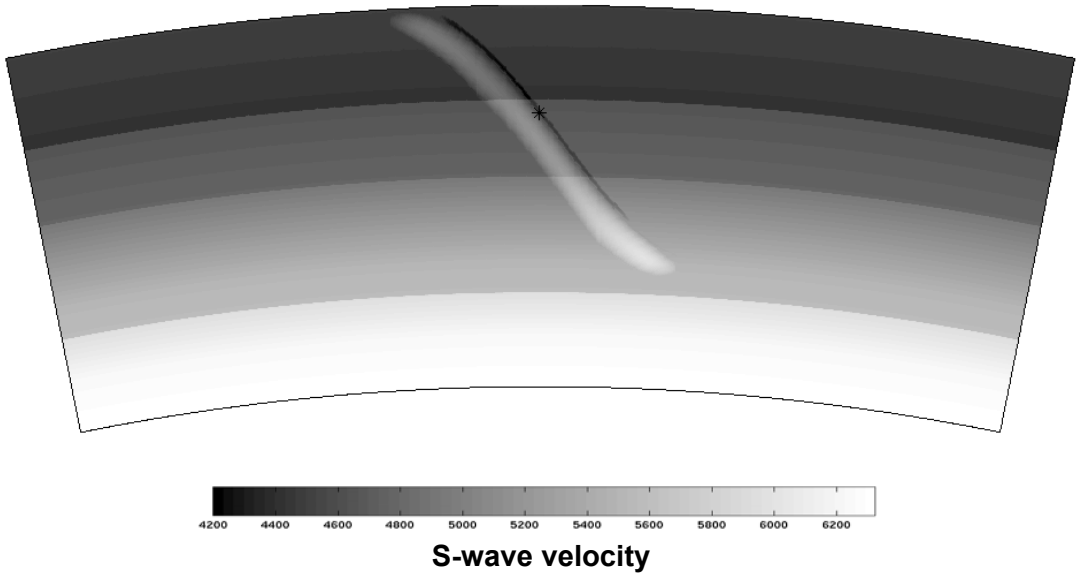

Figure 8: Vertical cross section through 3-D model at a plane θ=const. The colour scaling shows the S-wave velocity (in m /s). The slab is invariant in the φ direction and reaches down to a depth of 600km. The background model is PREM. The positive velocity perturbation towards the centre of the slab has a 8% maximum. A thin low velocity layer at the top of the subduction zone has a maximum negative perturbation of 4%. The source (*) is located inside this low velocity zone. The maximum depth is 808km and the horizontal range is 22° and 13° for φ– and θ-directions, respectively.

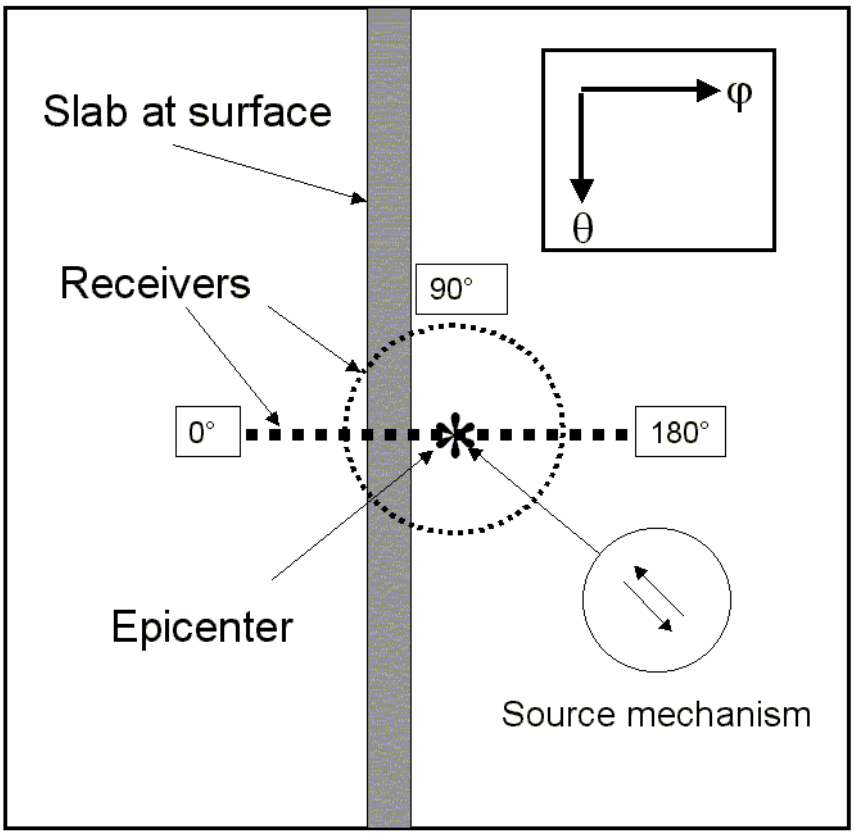

Figure 9: Schematic diagram of the receiver profile and ring at the surface. The receiver ring is at an epicentral distance of 5°. The azimuth is calculated clockwise from the φ-axis.

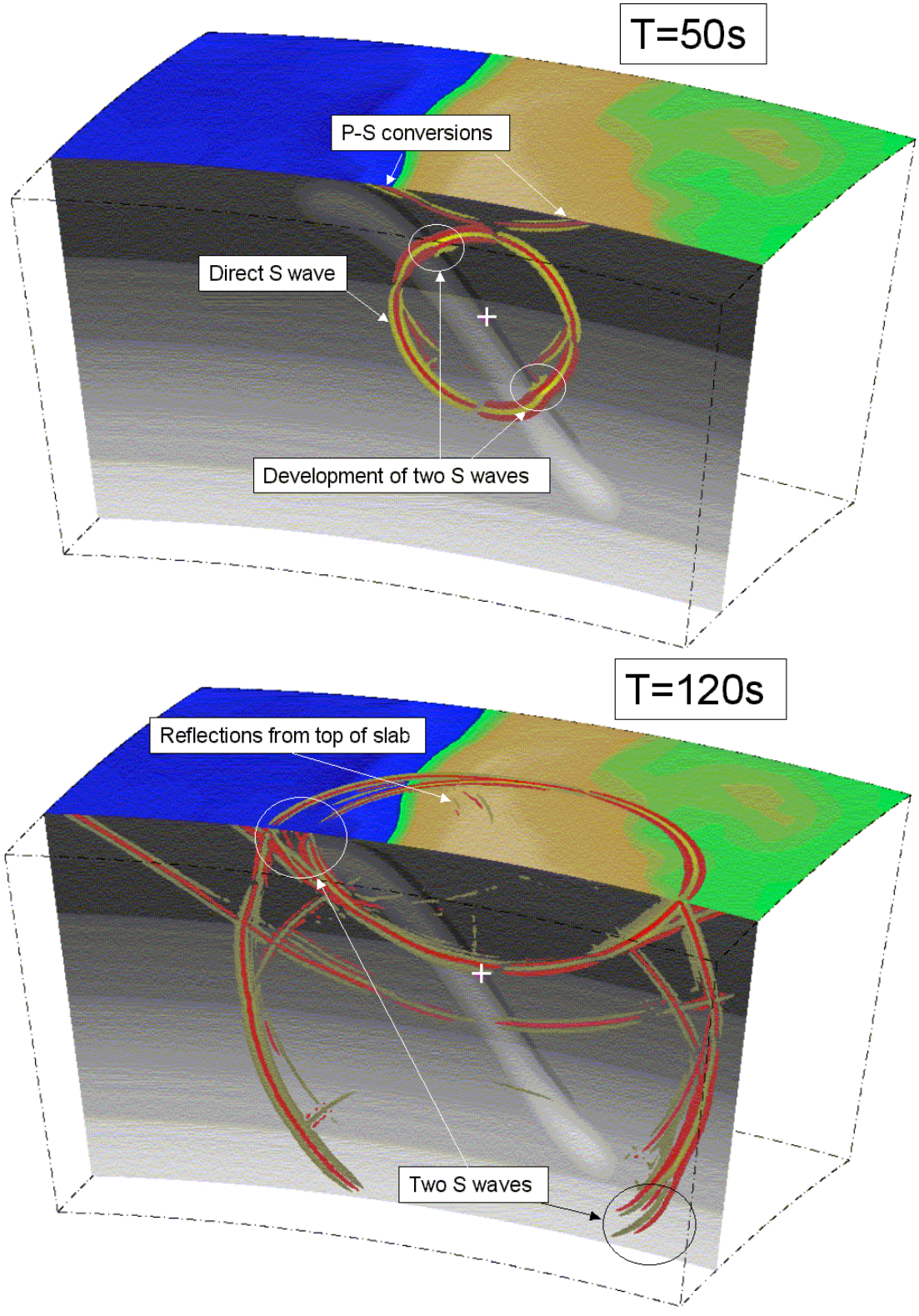

Figure 10: Snapshots of slab simulation. The component of the curl perpendicular to the relevant plane is shown. **Top:** Wavefield after 50s. Note the development of an additional shear wave within the slab due to the low-velocity zone. **Bottom:** Wavefield after 120s. In the direction of the slab two distinct shear phases develop. At the top of the slab shear waves are reflected in eastern direction. Coastlines of South America are superimposed.

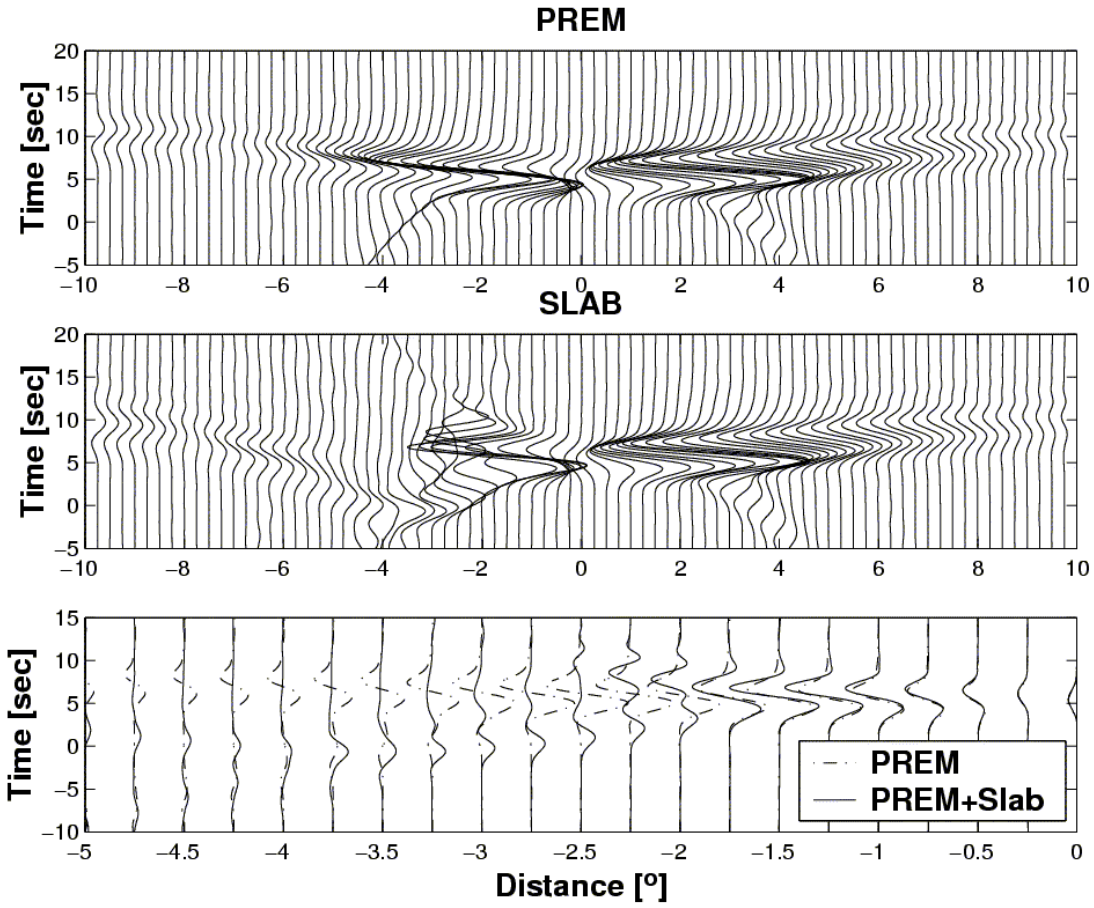

Figure 11: Synthetic seismograms (vertical-component) on a profile perpendicular to the strike of the subduction zone (along φ) through the epicenter. A 30s time window around the S-wave arrival is shown for both PREM and the laterally heterogeneous slab model. Note the phase effects for waves propagating inside the slab and the strong effects on the amplitudes and waveforms at distances around -2°.

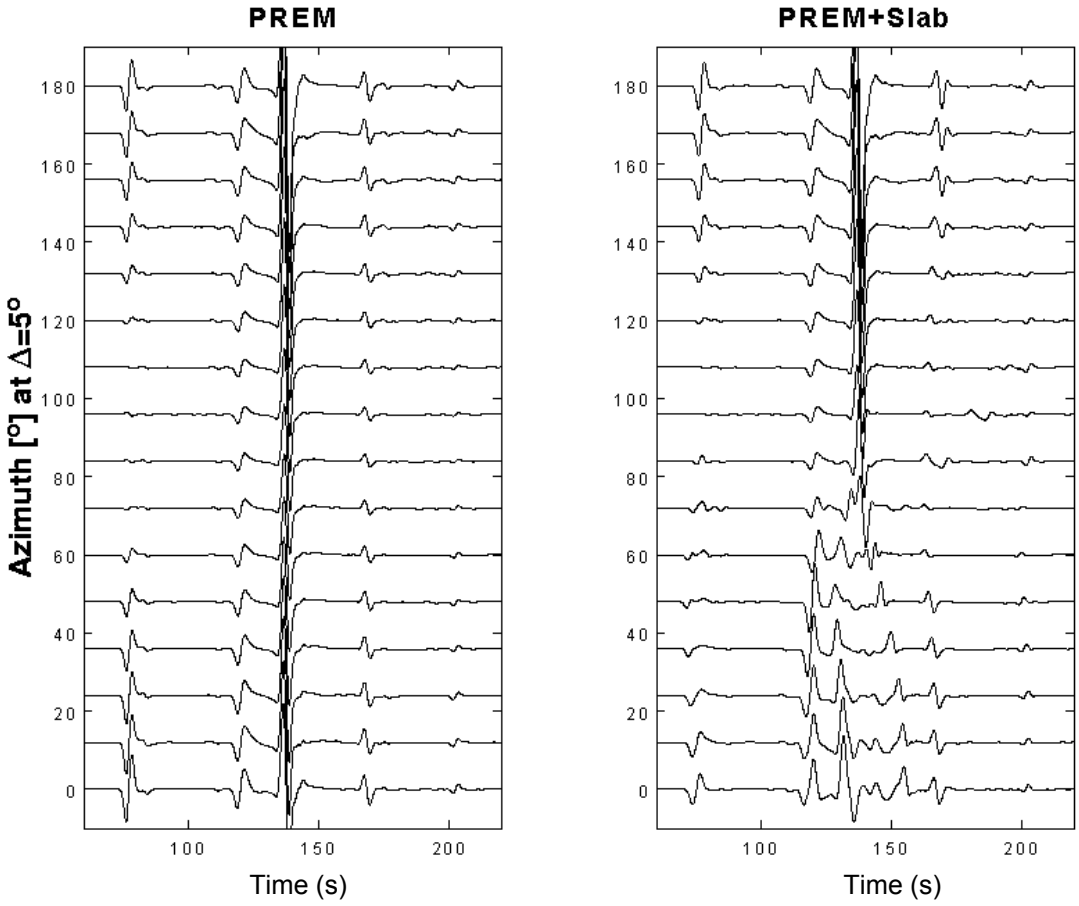

Figure 12: Synthetic seismograms (vertical component) recorded on a semi-ring at 5^{o} epicentral distance (W-N-E). The dominant period is 6 seconds. **Left:** seismograms for background model. **Right:** Seismograms for model with slab.

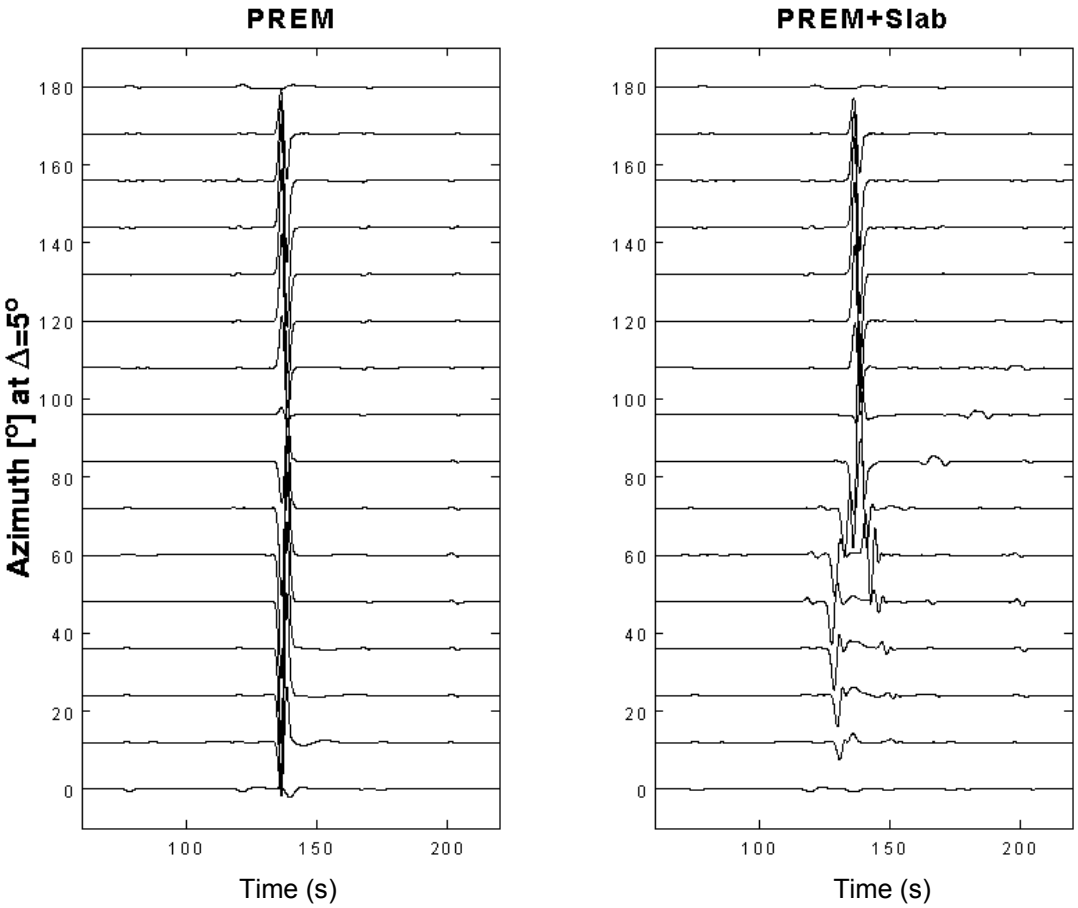

Figure 13: Synthetic seismograms (transverse component) recorded on a semi-ring at 5^{o} epicentral distance (W-N-E). The dominant period is 6 seconds. **Left:** seismograms for background model. **Right:** Seismograms for model with slab.